JMEPEG
https://doi.org/10.1007/s11665-023-09100-z

1059-9495/$19.00

ORIGINAL RESEARCH ARTICLE

Elastic Properties and Energy Absorption of Irregular Auxetic Cellular Structure

Xinru Zhang, Qingtian Deng, Xueli Song, and Xinbo Li

Submitted: 28 June 2023 / Revised: 11 November 2023 / Accepted: 27 November 2023

Based on Euler-Bernoulli beam theory, the equivalent elastic properties of auxetic cellular structure with irregular configurations are derived by using the representative unit cell element approach and multi-step bottom-up approach. Meanwhile, the effect of cell height and inclination angle on the in-plane linear elastic properties is explored. In addition, the Mechanical properties of the auxetic cellular structure with gradient cell height are analyzed under quasi-static compressive loading. The results show that the theoretical derivation results agree well with the results from available literature. The failure of all structures is the layer-by-layer collapse of cellular structural cells. The gradient cell size has little effect on the elastic phase of stress-strain behavior and energy absorption performance. The bidirectional gradient structure has higher platform stress compared with the unidirectional gradient structure. The homogeneous small size structure has the strongest load-bearing capacity as well as energy-absorbing performance. The structure, unidirectional gradient from large to small size, has the weakest load bearing capacity.

Keywords auxetic cellular structure, energy absorption, irregular, multi-step bottom-up approach, the representative unit cell element approach

1. Introduction

Cellular structures have been observed in many natural materials, e.g., wood and bamboo, and possess prominent mechanical performances (Ref 1-3). These kinds of materials have inspired novel design of engineered lightweight structures and have been employed in wave absorption materials (Ref 4, 5), sandwich panels (Ref 6), impact mitigation (Ref 7) and biomedical implants (Ref 8). The negative Poisson's ratio structures have been found to have excellent performance in terms of energy absorption, crashworthiness, and fatigue strength (Ref 9-11). Through arranging the cell geometry or varying-density, high performance artificial cellular structures can be manufactured in many ways (Ref 12-14), which can be divided into stochastic and periodic ones.

Conventional cellular structures have been presented in many literatures, especially auxetic cellular structures, which have been explored from atomic scale to macroscale. Zhang et al. (Ref 15, 16) investigated the effects of geometric parameters such as honeycomb size, porosity, and relative density on the crack resistance of porous structures. Tatl (Ref 17) investigated the In-plane dynamic behavior of double-arrow, re-entrant honeycomb, chiral, missing-slit, and star-assisted honeycomb structures by using finite element analysis. Novak et al. (Ref 18) evaluated the responses of chiral auxiliary cell structures in quasi-static and high strain rate by experimental tests. Auxetic behavior, which brings enhancements of engineering properties such as acoustic absorption capacity, double curvature stiffness and indentation resistance, can be observed or introduced in cellular structures by making suitable arrangements of micro-structural geometry. To evaluate the effective material properties of different structures having various configurations, it is common to use a representative unit cell to model entire cellular structures. Also, computational homogenization techniques are the most used method to characterize the responses of different regular cellular structures (Ref 19-22). Gao et al. (Ref 23) explored the elastic modulus and Poisson's ratio of a double-arrow structure using representative units and a top-down theoretical approach.

Although regular structures have been studied based on unit cell approach, structures with irregularity are inevitable due to manufacturing techniques, pre-stressing, temperature, and geometric variation. Several methods and models are found to be considered in literature. Hou et al. (Ref 24) proposed a new material for energy dissipation with a gradient consisting of auxetic cellular cells of different heights, and the results showed that the gradient structure has a lower resistance and better energy absorption capacity. Li et al. (Ref 25) present a novel optimization strategy for designing functionally graded cellular structures with desired mechanical properties. Novak et al. (Ref 26) proposed a new shape optimization procedure to develop new auxetic structures with functionally graded geometry, and with the introduction of functionally graded geometry, the response of the auxetic structure can be tailored to specific loading conditions. Niknam et al. (Ref 27) introduced concept of architected multi-directional functionally graded cellular materials, which are made by assembling porous unit cells of dissimilar densities and cell topologies and mechanical properties of related plates are predicted by using standard mechanics homogenization. Results showed cell variation through thickness is more effective than variation through length or width on structural responses. Niknam et al

Xinru Zhang, Qingtian Deng, Xueli Song, and **Xinbo Li**, School of Science, Chang'an University, Xi'an, China. Contact e-mails: dengqt@chd.edu.cn and sinboy1016@chd.edu.cn.

Published online: 03 January 2024

(Ref 28) studied the in-plane dynamic extrusion of two-dimensional honeycombs with regular hexagonal and irregular hexagonal arrangements using a detailed finite element model. Li et al. (Ref 29) investigated the mechanical behavior of biologically inspired functionally graded cellular structures under compressive loading and showed that graded honeycomb structures have better energy absorption than uniform structures.

Analytical approaches for quantifying the effect of irregularity in cellular structures have been reported for evaluate elastic properties (Ref 30-32). This paper discusses the problem of auxetic cellular structures with spatially irregular cell arrangement based on beam theory and multi-step bottom-up approach. The equivalent Young's modulus and equivalent Poisson's ratio of entire cellular structures are derived by assembled multiple numbers of representative unit cell elements. Analytical expressions are validated numerically with literature for regular auxetic and functionally graded cellular structures. The effect of cell height and inclination angle on the equivalent elastic properties of the structure is analyzed theoretically. Meanwhile, the deformation pattern, stress-strain behavior, and energy absorption performance of the auxetic cellular structure with gradient cell size under quasi-static compressive loading are investigated.

2. Irregular Auxetic Cellular Structure

Figure 1 shows a typical model of selected representative unit cell element (RUCE) from auxetic cellular structure, in which the four inclined cell walls with lengths having inclination angle, respectively. The two inclined cell walls and have inclination angle and in X_2 direction. The cell walls are considered as beam with thickness t and depth b, which are made of original material with Young's modulus E_s. In this paper, it is considered that the material is uniformly and continuously distributed in the structure.

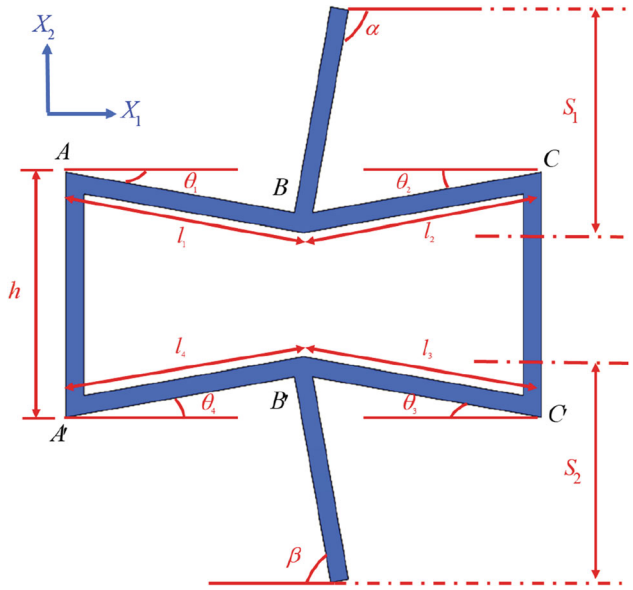

Fig. 1 A typical model of irregular auxetic RUCE

2.1 Equivalent Young's Modulus in X_1 Direction

The original length of RUCE in Fig. 1 along X_1 direction can be expressed as

$$\delta_{X1} = l_1 \cos\theta_1 + l_2 \cos\theta_2 \quad \text{(Eq 1)}$$

Assuming stress is applied in X_1 direction, the deformation of RUCE in X_1 direction can be obtained, then inclined cell wall BC is selected as shown in Fig. 2, in which each node has three degrees of freedom. The cell wall is modeled using Euler-Bernoulli beam, and axial deformation is not considered by assuming axial rigidity, and in Fig. 2 are the horizontal, vertical forces and moment at the nodes.

The moment act at node B can be expressed

$$M = \frac{P_1 l_2 \sin\theta_2}{2} = \frac{P_1 l_1 \sin\theta_1}{2} \quad \text{(Eq 2)}$$

where $P_1 = \sigma_1(h - l_1 \sin\theta_1)b$.

According to the standard beam theory and structural mechanics theory, the total deflections of section BC and BA in X_1 direction is

$$\begin{aligned}\delta_1 &= \frac{\frac{P_1}{n} l_1^3 \sin\theta_1}{12E_s I}\sin\theta_1 + \frac{\frac{P_1}{m} l_2^3 \sin\theta_2}{12E_s I}\sin\theta_2 \\ &= \frac{P_1}{6E_s I}\frac{l_1^3 l_2^3 \sin^2\theta_1 \sin^2\theta_2}{l_1^3 \sin^2\theta_1 + l_2^3 \sin^2\theta_2}\end{aligned} \quad \text{(Eq 3)}$$

where $n = 1 + \frac{\sin^2\theta_1 l_1^3}{\sin^2\theta_2 l_2^3}$, $m = 1 + \frac{\sin^2\theta_2 l_2^3}{\sin^2\theta_1 l_1^3}$, $I = \frac{bt^3}{12}$

The strain in X_1 direction is

$$\begin{aligned}\varepsilon_1 &= \frac{\delta_1}{\delta_{X1}} \\ &= \frac{\sigma_1(h - l_1\sin\theta_1)b}{6E_s I}\frac{l_1^3 l_2^3 \sin^2\theta_1 \sin^2\theta_2}{\left(l_1^3 \sin^2\theta_1 + l_2^3 \sin^2\theta_2\right)\left(l_1\cos\theta_1 + l_2\cos\theta_2\right)}\end{aligned} \quad \text{(Eq 4)}$$

The equivalent Young's modulus in X_1 direction for the RUCE can be expressed as

$$E_1 = \frac{\sigma_1}{\varepsilon_1} = \frac{E_s t^3\left(l_1^3 \sin^2\theta_1 + l_2^3 \sin^2\theta_2\right)\left(l_1\cos\theta_1 + l_2\cos\theta_2\right)}{2(h - l_1\sin\theta_1)l_1^3 l_2^3 \sin^2\theta_1 \sin^2\theta_2} \quad \text{(Eq 5)}$$

To derive expressions equivalent for elastic properties of the entire structure, the multi-step bottom-up approach is utilized (Ref 30, 31). The lengths of entire irregular cellular structure in direction X_1 and direction X_2 are L and B and is divided it into

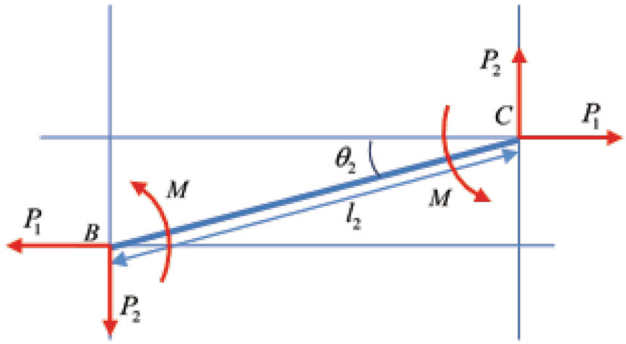

Fig. 2 Free body diagram of BC for equivalent Young's modulus in direction X_1

$m \times n$ number of RUCEs, which have m and n numbers of RUCEs in direction X_1 and X_2, respectively. A selected cell at ith column and jth row as shown in Fig. 3, where $i = 1, 2, \ldots, m$ and $j = 1, 2, \ldots, n$.

Then, the equivalent Young's modulus of jth strip $\overline{E}_{1j}$ in X_1 direction is obtained as

$$\overline{E}_{1j} = \frac{\sum_{i=1}^{m} \left(l_{1ij}\cos\theta_{1ij} + l_{2ij}\cos\theta_{2ij}\right)}{\sum_{i=1}^{m} \frac{\left(l_{1ij}\cos\theta_{1ij} + l_{2ij}\cos\theta_{2ij}\right)}{E_{1ij}}} \quad \text{(Eq 6)}$$

where l_{1ij} and l_{2ij} are the length of the cell walls having length l_1 and l_2 with the inclination angle θ_1 and θ_2 in the RUCE positioned at (i,j) as shown in Fig. 3, E_{1ij} is the equivalent Young's modulus of the RUCE positioned at (i,j) in direction X_1.

Following the approach, the equivalent Young's modulus E_{1eq} in direction X_1 of the entire irregular cellular structure can be obtained

$$E_{1eq} = \frac{1}{\left(\sum_{j=1}^{n} B_j\right)} \sum_{j=1}^{n} \left(\frac{\sum_{i=1}^{m} \left(l_{1ij}\cos\theta_{1ij} + l_{2ij}\cos\theta_{2ij}\right)}{\sum_{i=1}^{m} \frac{\left(l_{1ij}\cos\theta_{1ij} + l_{2ij}\cos\theta_{2ij}\right)}{E_{1ij}}} \right) B_j \quad \text{(Eq 7)}$$

where B_j is the height of the RUCE.

2.2 Equivalent Young's Modulus in X_2 Direction

The length of RUCE in Fig. 1 along X_2 direction is

$$\delta_{X2} = h + (s_1 - l_2\sin\theta_2) + (s_2 - l_3\sin\theta_3) \quad \text{(Eq 8)}$$

Assuming stress σ_2 is applied in X_2 direction, the deformation of RUCE in X_2 direction also can be obtained, then the inclined cells AB and BC are selected as shown in Fig. 4. The vertical force and moment act at joint B are $W = \sigma_2 b(l_1\cos\theta_1 + l_2\cos\theta_2)$ and $M_1 = W s_1 \cot\alpha$.

The bending deformation of the cell wall with inclination angle α in direction X_2 can be expressed as

$$\delta'_{21} = \left(\frac{W\cos\alpha\left(\frac{s_1}{\sin\alpha}\right)^3}{3E_sI} \right)\cos\alpha \quad \text{(Eq 9)}$$

where $I = bt^3/12$.

Substituting vertical force W into Eq 9, it has

$$\delta'_{21} = \frac{\sigma_2 b s_1^3 \cos^2\alpha(l_1\cos\theta_1 + l_2\cos\theta_2)}{3E_sI\sin^3\alpha} \quad \text{(Eq 10)}$$

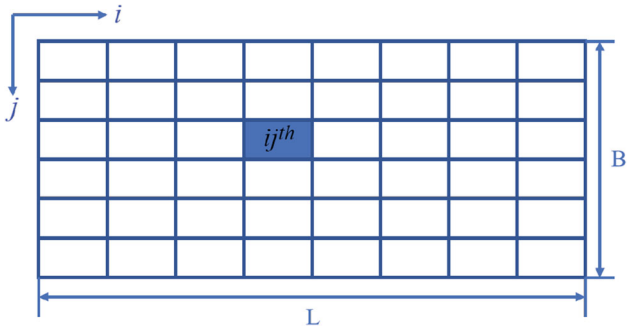

Fig. 3 Cellular structure with m × n number of RUCEs

By considering stiffness of the cell wall, moment acting on cell wall BC and BA can be expressed as the following

$$BC : M'_{1BC} = \frac{M_1}{1 + \frac{l_2}{l_1}} \quad \text{(Eq 11)}$$

$$BA : M'_{1BA} = \frac{M_1}{1 + \frac{l_1}{l_2}} \quad \text{(Eq 12)}$$

The angle of rotation at joint B is

$$\phi = \frac{M_1}{1 + \frac{l_2}{l_1}} \frac{l_2}{6E_sI} = \frac{\sigma_2 b l_1 l_2 (l_1\cos\theta_1 + l_2\cos\theta_2)\mathrm{s}_1\cot\alpha}{6E_sI(l_1 + l_2)} \quad \text{(Eq 13)}$$

The component of rotational deformation of the cell wall having inclination angle α in direction X_2 can be expressed as

$$\delta'_{22} = \phi\frac{s_1}{\sin\alpha}\cos\alpha \quad \text{(Eq 14)}$$

Substituting angle ϕ into Eq 14, it has

$$\delta'_{22} = \frac{\sigma_2 b l_1 l_2 (l_1\cos\theta_1 + l_2\cos\theta_2)\mathrm{s}_1^2\cot^2\alpha}{6E_sI(l_1 + l_2)} \quad \text{(Eq 15)}$$

Then, the total deformation in direction X_2 of the cell wall with inclination angle α can be expressed as

$$\delta'_2 = \delta'_{21} + \delta'_{22} = \frac{2\sigma_2 \mathrm{s}_1^2 (l_1\cos\theta_1 + l_2\cos\theta_2)}{E_s t^3}\left[\frac{2s_1\cos^2\alpha}{\sin^3\alpha} + \frac{l_1 l_2\cot^2\alpha}{(l_1 + l_2)}\right] \quad \text{(Eq 16)}$$

Similar with δ'_{21}, the bending deformation of the cell wall with inclination angle β in direction X_2 can be expressed as

$$\delta''_{21} = \left(\frac{W\cos\beta\left(\frac{s_2}{\sin\beta}\right)^3}{3E_sI} \right)\cos\beta \quad \text{(Eq 17)}$$

And moment act at joint B' is $M''_1 = W s_2 \cot\beta$.

By considering stiffness of the cell wall, moment acting on cell wall $B'C'$ and $B'A'$ can be expressed as the following

$$B'C' : M''_{1B'C'} = \frac{M''_1}{1 + \frac{l_3}{l_4}} \quad \text{(Eq 18)}$$

$$B'A' : M''_{1B'A'} = \frac{M''_1}{1 + \frac{l_4}{l_3}} \quad \text{(Eq 19)}$$

The angle of rotation is

$$\phi = \frac{M''_1}{1 + \frac{l_3}{l_4}} \frac{l_3}{6E_sI} \quad \text{(Eq 20)}$$

The component of rotational deformation of the cell wall with inclination angle β in direction X_2 can be expressed as

$$\delta''_{22} = \phi\frac{s_2}{\sin\beta}\cos\beta \quad \text{(Eq 21)}$$

Then, the total deformation in direction X_2 of the cell wall with inclination angle β in direction X_2 can be expressed as

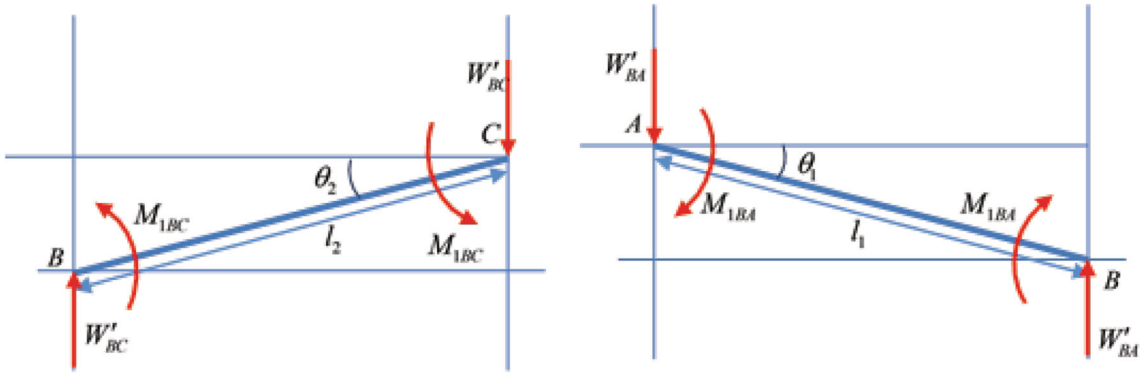

Fig. 4 Free body diagram of *BC* and *AB* for equivalent Young's modulus in direction X_2

$$\delta''_2=\delta''_{21}+\delta''_{22}=\frac{2\sigma_2 s_2^2(l_3\cos\theta_3+l_4\cos\theta_4)}{E_s t^3}\left[\frac{2s_2\cos^2\beta}{\sin^3\beta}+\frac{l_3 l_4\cot^2\beta}{(l_3+l_4)}\right] \quad \text{(Eq 22)}$$

The deformation of cell walls with inclination angle θ_1 and θ_4 in direction X_2 can be expressed as

$$\delta'''_{21}=\frac{\left(\frac{W}{n}\cos\theta_1\right)l_1^3}{12E_s I}\cos\theta_1 \quad \text{(Eq 23)}$$

$$\delta'''_{22}=\frac{\left(\frac{W}{\mathrm{m}}\cos\theta_4\right)l_4^3}{12E_s I}\cos\theta_4 \quad \text{(Eq 24)}$$

where $W'''_{BC}=\frac{W}{\mathrm{n}}=\frac{W}{1+\frac{\cos^2\theta_1 l_1^3}{\cos^2\theta_2 l_2^3}}$, $W'''_{BA}=\frac{W}{m}=\frac{W}{1+\frac{\cos^2\theta_4 l_4^3}{\cos^2\theta_3 l_3^3}}$, $\mathrm{n}=1+\frac{\cos^2\theta_1 l_1^3}{\cos^2\theta_2 l_2^3}$, $\mathrm{m}=1+\frac{\cos^2\theta_4 l_4^3}{\cos^2\theta_3 l_3^3}$.

Then, Eq 23, 24 can be rewritten as

$$\delta'''_{21}=\frac{\sigma_2(l_1\cos\theta_1+l_2\cos\theta_2)\cos^2\theta_2 l_2^3\cos^2\theta_1 l_1^3}{E_s\left(\cos^2\theta_1 l_1^3+\cos^2\theta_2 l_2^3\right)t^3} \quad \text{(Eq 25)}$$

$$\delta'''_{22}=\frac{\sigma_2(l_3\cos\theta_3+l_4\cos\theta_4)\cos^2\theta_3 l_3^3\cos^2\theta_4 l_4^3}{E_s\left(\cos^2\theta_3 l_3^3+\cos^2\theta_4 l_4^3\right)t^3} \quad \text{(Eq 26)}$$

$$\delta'''_2=\delta'''_{21}+\delta'''_{22}=\frac{\sigma_2}{E_s t^3}\left[\frac{(l_1\cos\theta_1+l_2\cos\theta_2)\cos^2\theta_2 l_2^3\cos^2\theta_1 l_1^3}{\left(\cos^2\theta_1 l_1^3+\cos^2\theta_2 l_2^3\right)}+\frac{(l_3\cos\theta_3+l_4\cos\theta_4)\cos^2\theta_3 l_3^3\cos^2\theta_4 l_4^3}{\left(\cos^2\theta_3 l_3^3+\cos^2\theta_4 l_4^3\right)}\right] \quad \text{(Eq 27)}$$

The total deformation of the RUCE in X_2 direction

$$\begin{aligned}\delta_2&=\delta'_2+\delta''_2+\delta'''_2\\&=\frac{2\sigma_2 s_1^2(l_1\cos\theta_1+l_2\cos\theta_2)}{E_s t^3}\left[\frac{2s_1\cos^2\alpha}{\sin^3\alpha}+\frac{l_1 l_2\cot^2\alpha}{(l_1+l_2)}\right]\\&+\frac{2\sigma_2 s_2^2(l_3\cos\theta_3+l_4\cos\theta_4)}{E_s t^3}\left[\frac{2s_2\cos^2\beta}{\sin^3\beta}+\frac{l_3 l_4\cot^2\beta}{(l_3+l_4)}\right]\\&+\frac{\sigma_2}{E_s t^3}\left[\frac{(l_1\cos\theta_1+l_2\cos\theta_2)\cos^2\theta_2 l_2^3\cos^2\theta_1 l_1^3}{\left(\cos^2\theta_1 l_1^3+\cos^2\theta_2 l_2^3\right)}+\frac{(l_3\cos\theta_3+l_4\cos\theta_4)\cos^2\theta_3 l_3^3\cos^2\theta_4 l_4^3}{\left(\cos^2\theta_3 l_3^3+\cos^2\theta_4 l_4^3\right)}\right]\end{aligned} \quad \text{(Eq 28)}$$

The strain along X_2 direction is

$$\varepsilon_2=\frac{\delta_2}{\delta_{X2}}=\frac{\left\{\begin{aligned}&\frac{2\sigma_2 s_1^2(l_1\cos\theta_1+l_2\cos\theta_2)}{E_s t^3}\left[\frac{2s_1\cos^2\alpha}{\sin^3\alpha}+\frac{l_1 l_2\cot^2\alpha}{(l_1+l_2)}\right]+\frac{2\sigma_2 s_2^2(l_3\cos\theta_3+l_4\cos\theta_4)}{E_s t^3}\left[\frac{2s_2\cos^2\beta}{\sin^3\beta}+\frac{l_3 l_4\cot^2\beta}{(l_3+l_4)}\right]\\&+\frac{\sigma_2}{E_s t^3}\left[\frac{(l_1\cos\theta_1+l_2\cos\theta_2)\cos^2\theta_2 l_2^3\cos^2\theta_1 l_1^3}{\left(\cos^2\theta_1 l_1^3+\cos^2\theta_2 l_2^3\right)}+\frac{(l_3\cos\theta_3+l_4\cos\theta_4)\cos^2\theta_3 l_3^3\cos^2\theta_4 l_4^3}{\left(\cos^2\theta_3 l_3^3+\cos^2\theta_4 l_4^3\right)}\right]\end{aligned}\right\}}{h+(s_1-l_2\sin\theta_2)+(s_2-l_3\sin\theta_3)} \quad \text{(Eq 29)}$$

The total deformation of cell walls with inclination angle θ_1 and θ_4 in direction X_2 can be expressed as

The equivalent Young's modulus in direction X_2 for RUCE can be written as

$$E_2 = \frac{\sigma_2}{\varepsilon_2} = E_s t^3 \frac{h + (s_1 - l_2 \sin\theta_2) + (s_2 - l_3 \sin\theta_3)}{\left\{ \begin{array}{r} 2s_1^2 (l_1 \cos\theta_1 + l_2 \cos\theta_2) \left[\frac{2s_1 \cos^2\alpha}{\sin^3\alpha} + \frac{l_1 l_2 \cot^2\alpha}{(l_1 + l_2)} \right] + 2s_2^2 (l_3 \cos\theta_3 + l_4 \cos\theta_4) \left[\frac{2s_2 \cos^2\beta}{\sin^3\beta} + \frac{l_3 l_4 \cot^2\beta}{(l_3 + l_4)} \right] \\ + \left[\frac{(l_1 \cos\theta_1 + l_2 \cos\theta_2) \cos^2\theta_2 l_2^3 \cos^2\theta_1 l_1^3}{\left(\cos^2\theta_1 l_1^3 + \cos^2\theta_2 l_2^3\right)} + \frac{(l_3 \cos\theta_3 + l_4 \cos\theta_4) \cos^2\theta_3 l_3^3 \cos^2\theta_4 l_4^3}{\left(\cos^2\theta_3 l_3^3 + \cos^2\theta_4 l_4^3\right)} \right] \end{array} \right\}} \quad \text{(Eq 30)}$$

The equivalent Young's modulus of jth strip $\overline{E}_{2j}$ in X_2 direction is

$$\overline{E}_{2j} = \frac{\sum_{i=1}^{m} E_{2ij} \left(l_{1ij} \cos\theta_{1ij} + l_{2ij} \cos\theta_{2ij} \right)}{\sum_{i=1}^{m} \left(l_{1ij} \cos\theta_{1ij} + l_{2ij} \cos\theta_{2ij} \right)} \quad \text{(Eq 31)}$$

where E_{2ij} is the equivalent Young's modulus of the RUCE positioned at (i,j) in direction X_2.

The equivalent Young's modulus E_{2eq} in direction X_2 of the entire irregular cellular structure is obtained

$$E_{2eq} = \frac{1}{\left[\sum_{j=1}^{n} B_j \frac{\sum_{i=1}^{m} \left(l_{1ij} \cos\theta_{1ij} + l_{2ij} \cos\theta_{2ij} \right)}{\sum_{i=1}^{m} E_{2ij} \left(l_{1ij} \cos\theta_{1ij} + l_{2ij} \cos\theta_{2ij} \right)} \right]} \left(\sum_{j=1}^{n} B_j \right) \quad \text{(Eq 32)}$$

2.3 Equivalent Poisson's Ratio

According to the definition, equivalent Poisson's ratio of a RUCE with loading in direction X_1 can be expressed as

$$\upsilon_{12} = -\frac{\varepsilon_2}{\varepsilon_1} \quad \text{(Eq 33)}$$

where $\varepsilon_1 = \frac{\delta_1}{\delta} = \frac{P(l_1^3 \sin^2\theta_1 + l_2^3 \sin^2\theta_2)}{12 E_s I (l_1 \cos\theta_1 + l_2 \cos\theta_2)}$

$$\varepsilon_2 = \frac{\delta_2}{\delta} = \frac{P l_1^3 \sin\theta_1 \cos\theta_1 + P l_2^3 \sin\theta_2 \cos\theta_2}{12 E_s I [h + (s_1 - l_2 \sin\theta_2) + (s_2 - l_3 \sin\theta_3)]}$$

Then, Eq 33 can be rewritten as

$$\upsilon_{12} = -\frac{\varepsilon_2}{\varepsilon_1} = -\frac{(l_1^3 \sin\theta_1 \cos\theta_1 + l_2^3 \sin\theta_2 \cos\theta_2)(l_1 \cos\theta_1 + l_2 \cos\theta_2)}{[h + (s_1 - l_2 \sin\theta_2) + (s_2 - l_3 \sin\theta_3)](l_1^3 \sin^2\theta_1 + l_2^3 \sin^2\theta_2)} \quad \text{(Eq 34)}$$

Equivalent Poisson's ratio of jth strip is

$$\overline{\upsilon}_{12j} = \frac{\sum_{i=1}^{m} \left(l_{1ij} \cos\theta_{1ij} + l_{2ij} \cos\theta_{2ij} \right)}{\sum_{i=1}^{m} \frac{\left(l_{1ij} \cos\theta_{1ij} + l_{2ij} \cos\theta_{2ij} \right)}{\upsilon_{12ij}}} \quad \text{(Eq 35)}$$

where υ_{12ij} is the equivalent Poisson's ratio of the RUCE positioned at (i,j) in direction X_1.

The equivalent Poisson's ratio υ_{12eq} of the entire irregular cellular structure is written as

$$\upsilon_{12eq} = \frac{\sum_{j=1}^{n} \left[\frac{\sum_{i=1}^{m} \left(l_{1ij} \cos\theta_{1ij} + l_{2ij} \cos\theta_{2ij} \right)}{\sum_{i=1}^{m} \frac{\left(l_{1ij} \cos\theta_{1ij} + l_{2ij} \cos\theta_{2ij} \right)}{\upsilon_{12ij}}} \right] B_j}{\sum_{j=1}^{n} B_j} \quad \text{(Eq 36)}$$

Equivalent Poisson's ratio of a RUCE for loading in direction X_2 is

$$\upsilon_{21} = -\frac{\varepsilon_1}{\varepsilon_2} \quad \text{(Eq 37)}$$

where

$$\varepsilon_1 = \frac{\delta_1}{\delta} = \frac{\sigma_2 \cos^2\theta_2 l_2^3 \sin\theta_1 \cos\theta_1 l_1^3}{E_s t^3 \left(\cos^2\theta_1 l_1^3 + \cos^2\theta_2 l_2^3\right)} + \frac{\sigma_2 \cos^2\theta_3 l_3^3 \sin\theta_4 \cos\theta_4 l_4^3}{E_s t^3 \left(\cos^2\theta_4 l_4^3 + \cos^2\theta_3 l_3^3\right)}$$

$$\varepsilon_2 = \frac{\delta_2}{\delta} = \frac{\left\{ \begin{array}{r} \frac{2\sigma_2 s_1^2 (l_1 \cos\theta_1 + l_2 \cos\theta_2)}{E_s t^3} \left[\frac{2s_1 \cos^2\alpha}{\sin^3\alpha} + \frac{l_1 l_2 \cot^2\alpha}{(l_1 + l_2)} \right] + \frac{2\sigma_2 s_2^2 (l_3 \cos\theta_3 + l_4 \cos\theta_4)}{E_s t^3} \left[\frac{2s_2 \cos^2\beta}{\sin^3\beta} + \frac{l_3 l_4 \cot^2\beta}{(l_3 + l_4)} \right] \\ + \frac{\sigma_2}{E_s t^3} \left[\frac{(l_1 \cos\theta_1 + l_2 \cos\theta_2) \cos^2\theta_2 l_2^3 \cos^2\theta_1 l_1^3}{\left(\cos^2\theta_1 l_1^3 + \cos^2\theta_2 l_2^3\right)} + \frac{(l_3 \cos\theta_3 + l_4 \cos\theta_4) \cos^2\theta_3 l_3^3 \cos^2\theta_4 l_4^3}{\left(\cos^2\theta_3 l_3^3 + \cos^2\theta_4 l_4^3\right)} \right] \end{array} \right\}}{h + (s_1 - l_2 \sin\theta_2) + (s_2 - l_3 \sin\theta_3)}$$

$$\upsilon_{21} = -\frac{\varepsilon_1}{\varepsilon_2} = -\frac{\dfrac{\sigma_2 \cos^2\theta_2 l_2^3 \sin\theta_1 \cos\theta_1 l_1^3}{E_s t^3\left(\cos^2\theta_1 l_1^3 + \cos^2\theta_2 l_2^3\right)} + \dfrac{\sigma_2 \cos^2\theta_3 l_3^3 \sin\theta_4 \cos\theta_4 l_4^3}{E_s t^3\left(\cos^2\theta_4 l_4^3 + \cos^2\theta_3 l_3^3\right)}}{\left\{\begin{array}{l}\dfrac{2\sigma_2 s_1^2(l_1\cos\theta_1 + l_2\cos\theta_2)}{E_s t^3}\left[\dfrac{2s_1\cos^2\alpha}{\sin^3\alpha} + \dfrac{l_1 l_2\cot^2\alpha}{(l_1+l_2)}\right] + \dfrac{2\sigma_2 s_2^2(l_3\cos\theta_3 + l_4\cos\theta_4)}{E_s t^3}\left[\dfrac{2s_2\cos^2\beta}{\sin^3\beta} + \dfrac{l_3 l_4\cot^2\beta}{(l_3+l_4)}\right] \\ + \dfrac{\sigma_2}{E_s t^3}\left[\dfrac{(l_1\cos\theta_1 + l_2\cos\theta_2)\cos^2\theta_2 l_2^3\cos^2\theta_1 l_1^3}{\left(\cos^2\theta_1 l_1^3 + \cos^2\theta_2 l_2^3\right)} + \dfrac{(l_3\cos\theta_3 + l_4\cos\theta_4)\cos^2\theta_3 l_3^3\cos^2\theta_4 l_4^3}{\left(\cos^2\theta_3 l_3^3 + \cos^2\theta_4 l_4^3\right)}\right]\end{array}\right\}}{h + (s_1 - l_2\sin\theta_2) + (s_2 - l_3\sin\theta_3)}$$

(Eq 38)

Then, Eq 37 can be rewritten as

Equivalent Poisson's ratio of a RUCE is

$$\overline{\upsilon}_{21j} = \frac{\sum_{i=1}^{m}\upsilon_{21ij}\left(l_{1ij}\cos\theta_{1ij} + l_{2ij}\cos\theta_{2ij}\right)}{\sum_{i=1}^{m}\left(l_{1ij}\cos\theta_{1ij} + l_{2ij}\cos\theta_{2ij}\right)} \quad \text{(Eq 39)}$$

where υ_{21ij} is the equivalent Poisson's ratio of the RUCE positioned at (i,j) in direction X_2.

Also, the equivalent Poisson's ratio υ_{21eq} of the entire irregular cellular structure is written as

$$\upsilon_{21\text{eq}} = \frac{\sum_{j=1}^{n} B_j}{\sum_{j=1}^{n}\frac{\sum_{i=1}^{m}\left(l_{1ij}\cos\theta_{1ij}+l_{2ij}\cos\theta_{2ij}\right)}{\sum_{i=1}^{m}\upsilon_{21ij}\left(l_{1ij}\cos\theta_{1ij}+l_{2ij}\cos\theta_{2ij}\right)}B_j} \quad \text{(Eq 40)}$$

To validate the expressions obtained in Sect. 2 theoretically, results from Gibson and Ashby (Ref 33) are introduced, which they have presented the analytical model for in-plane elastic properties of 2D honeycomb with identical thickness vertical and diagonal ribs as shown in Fig. 5. The relative equivalent Young's modulus and equivalent Poisson's ratio are given as

$$\begin{cases}\frac{E_1^*}{E_s} = \left(\frac{t}{l}\right)^3\frac{\cos\theta}{(h/l+\sin\theta)\sin^2\theta} \\ \frac{E_2^*}{E_s} = \left(\frac{t}{l}\right)^3\frac{(h/l+\sin\theta)}{\cos^3\theta} \\ \upsilon_{12}^* = \frac{\cos^2\theta}{(h/l+\sin\theta)\sin\theta} \\ \upsilon_{21}^* = \frac{(h/l+\sin\theta)\sin\theta}{\cos^2\theta}\end{cases} \quad \text{(Eq 41)}$$

If four inclined cell walls of the RUCE shows in Fig. 1 have same lengths $l_1 = l_2 = l_3 = l_4$ and having same inclination angle $\theta_1 = \theta_2 = \theta_3 = \theta_4$, also $\alpha = \beta = 90^\circ$ and $s_1 = s_2 = h/2$, the expressions of equivalent Young's modulus and equivalent Poisson's ratio in Eq. 5, 30, 34 and 38 can be reduced to expressions in Eq 41.

2.4 Effects of Geometrical Parameters on Elastic Properties of Auxetic Cellular Structures

To explore the effect of geometrical parameters on the in-plane linear elastic properties of auxetic cellular structures, numerical computation has een performed in this paper. Full-scale models consisting of 6×8 unit cells and the elements used in the models have a constant thickness $t = 1$ mm.

2.4.1 Unit height h varying from 5.5mm to 8mm with a step 0.5mm ($l_1 = l_2 = l_3 = l_4 = 9.65$ mm, $\theta_1 = \theta_2 = \theta_3 = \theta_4 = 10^\circ$, $\alpha = \beta = 90^\circ$). Figure 6 shows the numerical computation consequence of the unit height. It can be observed that the variation of unit height has a significant effect on the non-dimensional equivalent Young's modulus $E_{1\text{eq}}/E_s$ and $E_{2\text{eq}}/E_s$ as well as the equivalent poisson's ratio $\upsilon_{12\text{eq}}$ and $\upsilon_{21\text{eq}}$. $E_{1\text{eq}}/E_s$ gradually decreases from 1.62942 to 1.16143 with the increase in unit height, and the reduction range gradually decreases, while $E_{2\text{eq}}/E_s$ increases from 0.0383 to 0.0632 with the increase in unit height. As the unit height increases from 5.5 mm to 8 mm, $\upsilon_{12\text{eq}}$ increases from − 8.68695 to − 6.19194 and the increase range gradually decreases, while the $\upsilon_{21\text{eq}}$ decreased from − 0.115115 to − 0.161500.

2.4.2 Inclination angle θ varying from 10° to 25° with a step 3° ($l_1 = l_2 = l_3 = l_4 = 9.65$ mm, $\alpha = \beta = 90^\circ$, $h = 5.5$mm. From Fig. 7, it can be concluded that inclination angle θ shows significant effects on the non-dimensional equivalent Young's modulus $E_{1\text{eq}}/E_s$ and $E_{2\text{eq}}/E_s$. $E_{1\text{eq}}/E_s$ exhibits a continuous increase from 39.28937 to 109.97178

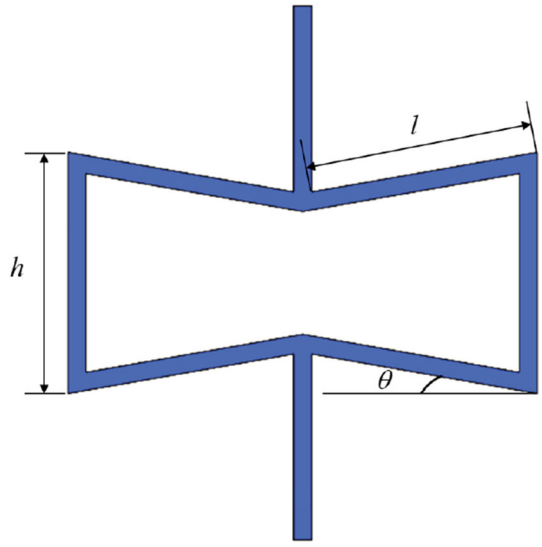

Fig. 5 2D auxetic honeycomb in Gibson and Ashby (Ref 30)

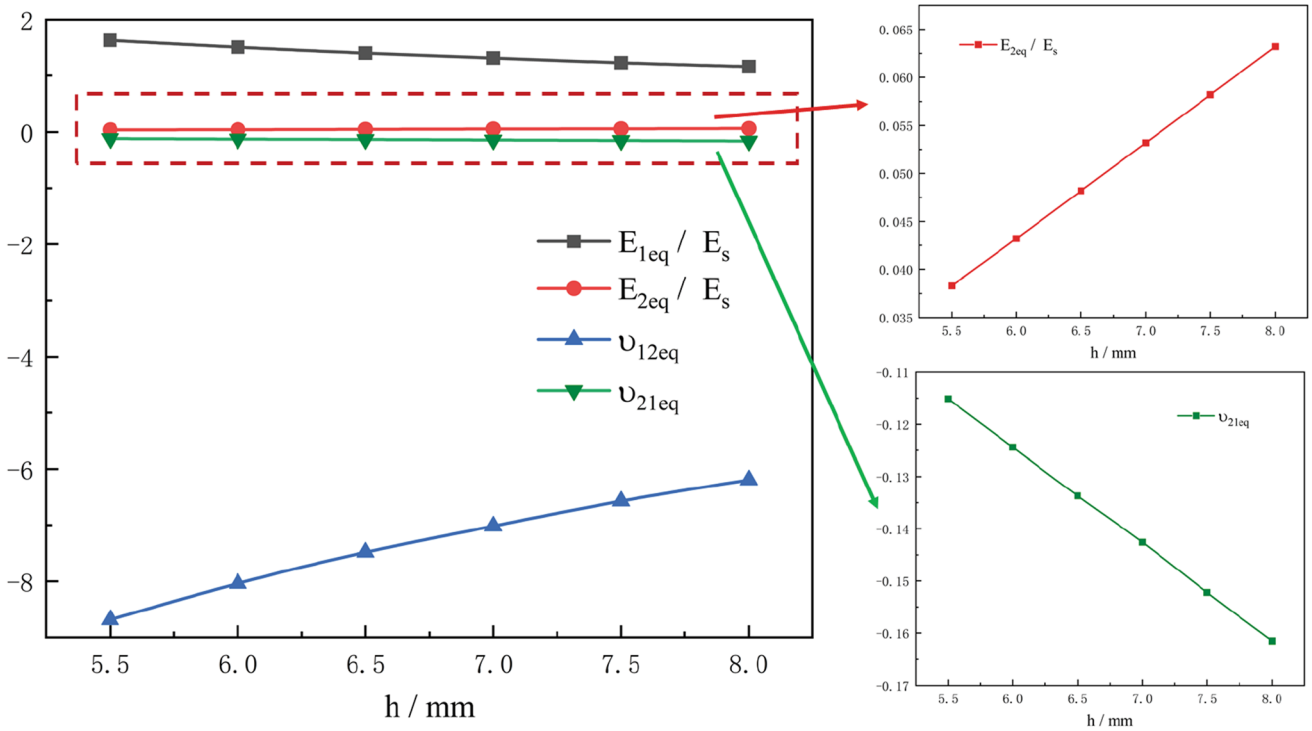

Fig. 6 Effects of unit height h on elastic properties

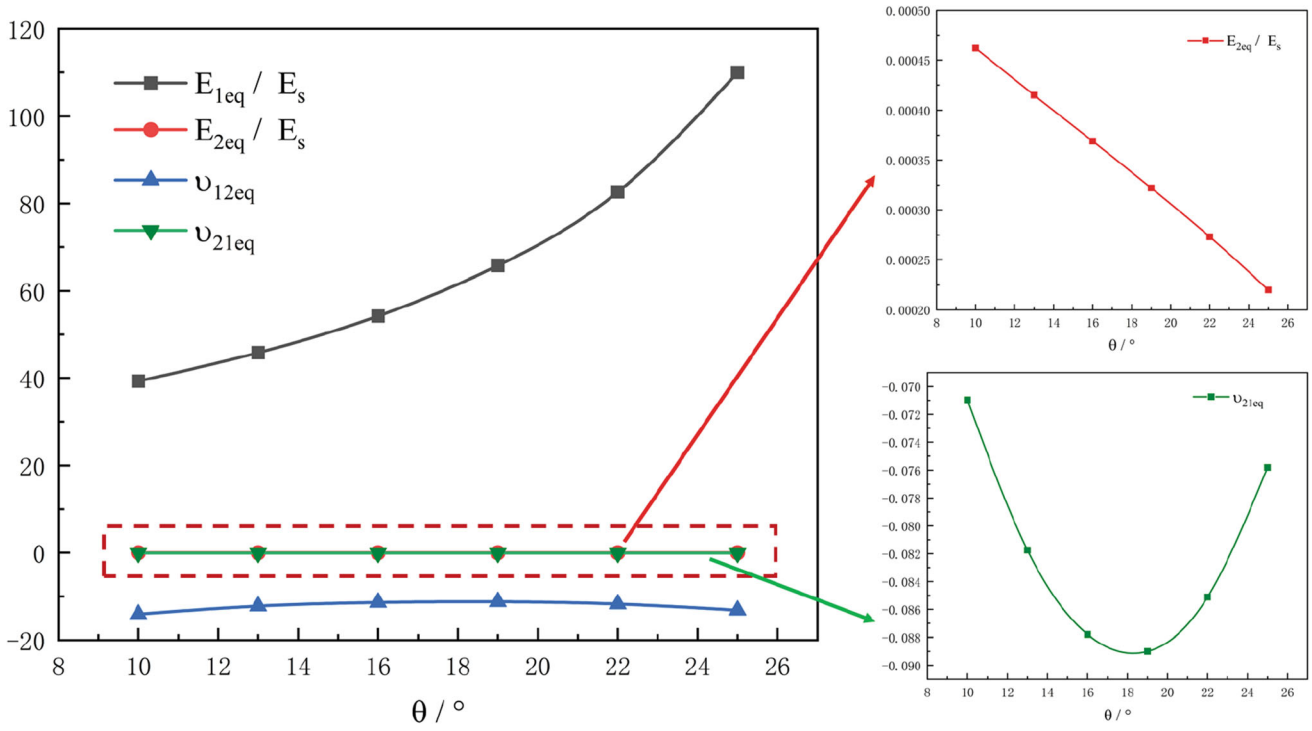

Fig. 7 Effects of inclination angle θ on elastic properties

with the inclination angle from 10° to 25°, and the increase amplitude gradually became larger. The value of E_{2eq}/E_s is in the range of approximately 10^{-4} and exhibits a continuous decrease with the inclination angle from 10° to 25°, and the decrease amplitude also gradually became larger. υ_{12eq} tends to increase and then decrease with the increase in inclination

angle, while υ_{21eq} tends to decrease and then increase with the increase in inclination angle, and both obtain the maximum value at 19°.

To further investigate the effect of unit height on the irregular auxetic cellular structure, quasi-static compression tests are completed as a means to investigate the effect of unit height gradient on the mechanical properties of the structure.

3. Quasi-static Compression Experiment of Auxetic Cellular Structure

3.1 Model Design

Auxetic cellular structure unit cells are typically defined by four parameters as shown in Fig. 8(a), including cell wall thickness t, unit height h, strut angle θ and unit lenght L. In this study, auxetic cellular structure unit cells are assembled into a 6×8 layered as shown in Fig. 8(b). The deformation mode and energy absorption under quasi-static compression with the change in unit height h are studied. The global width W of 145.11mm and out-of-plane depth of 15mm, the global height may vary slightly and are detailed listed in Table 1. By varying the parameter of unit height, graded auxetic cellular structure can be attained as shown in Fig. 8(c).

Two main gradient directions are incorporated in this present study: unidirectional and bidirectional gradient. For the unidirectional gradient structure, the 0.5mm gradient is used to increase or decrease from the distal end to the proximal end, respectively, as shown in Fig. 8(c3) and Fig. 8(c4). LS represents a decreasing gradient from proximal to distal, in contrast, SL represents a gradual increase in gradient from proximal to distal. For the bidirectional gradient structure, the central layer is used to increase or decrease the 0.5mm gradient symmetrically toward both ends as shown in Fig. 8(c5) and Fig. 8(c6). LSL represents the gradient gradually increasing from the middle layer to both ends, while SLS represents the radient gradually decreasing from the middle layer to both ends. The gradient direction can be identified by the blue symbols on the left side of each structure as shown in Fig. 8(c). The detailed characteristic parameters of each structure are documented in Table 1.

3.2 Specimen Manufacturing

The 3D printing fused deposition molding (FDM) technology is used for the manufacturing of the specimens, the basic principle of which is to warm up the raw hot molten filament to a molten state by means of electrical heating, followed by computer software that uses a nozzle with a diameter of 0.4 mm to extrude the molten filament to achieve layer-by-layer accumulation of the melt, thus achieving three-dimensional molding.

Biodegradable plastic polylactic acid (PLA) has become the main material for FDM rapid prototyping technology due to its easy adhesion and ductility after melting, odorless printing and almost no shrinkage of the printed material. Therefore, PLA is adopted in this paper as the raw material for 3D printing to prepare gradient auxetic cellular specimens. Figure 9 shows the prepared specimens.

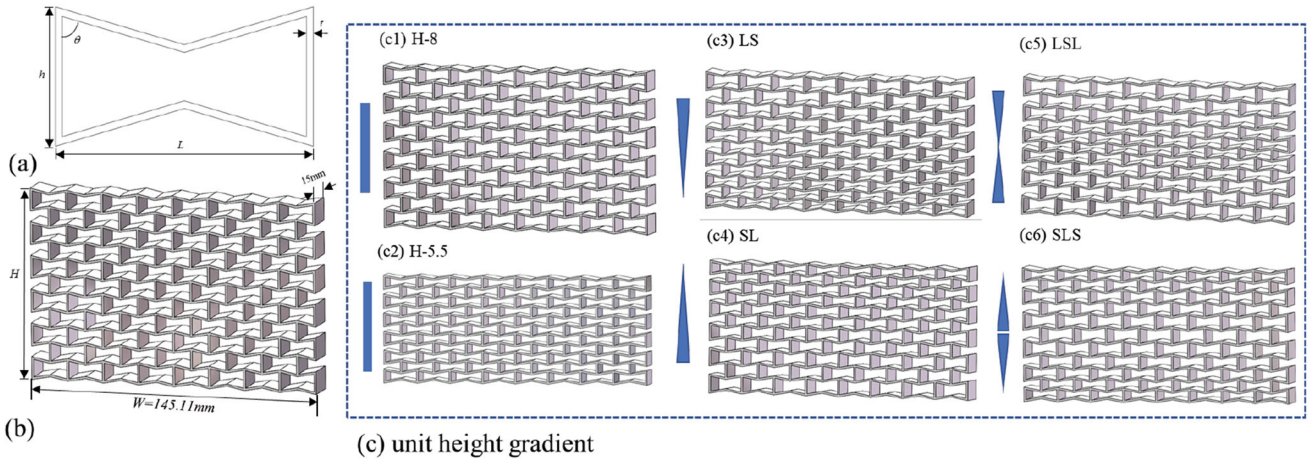

Fig. 8 (a) Depiction of auxetic unit cell (b) Visualization of uniform control models with h = 8mm (c) Unit height gradient auxetic cellular structure

Table 1 Detailed parameters of the structure

Structure	h, mm	H, mm	θ, °	L, mm	t, mm	Weight, g	Porosity, %
H-8	8	86.42	80	18.01	0.5	39.47	79.83
H-5.5	5.5	58.56	80	18.01	0.5	38.56	72.93
LS	8–5.5	73.92	80	18.01	0.5	40.62	77.42
SL	5.5–8	71.42	80	18.01	0.5	40.16	76.82
LSL	8–5.5–8	73.92	80	18.01	0.5	40.66	77.41
SLS	5.5–8–5.5	71.39	80	18.01	0.5	39.87	76.87

3.3 Experimental Testing

The quasi-static compression test loading device of this experiment is shown in Fig. 10, which consists an observation system and a loading system. In this study, compression tests are performed using CMT5305 universal testing machine and the loading rate is 2mm/min. The compression test is recorded with a high-resolution camera. Before loading, the specimens are left at room temperature to dry and then are polished with sandpaper in the top and bottom ends to reduce the end effect due to friction generated by the uneven surface of the specimens. During the experiment, the computer will record the stress-strain curve data of the test in real time, automatically calculate various parameters and generate relevant curves.

4. Results and Discussion

The mechanical responses of all four graded auxetic honeycombs under in-plane quasi-static compression are discussed. The deformation patterns, stress-strain behavior and energy absorption performance are compared and analyzed between different gradient directions. An in-depth research of unit cells in the homogeneous auxetic structure was detailed in our previous work. Here, for gradient-based auxetic structures, both micro and meso-deformation will be used to evaluate the collapse pattern throughout the compression.

4.1 Deformation Patterns

For all structures, only slight lateral shrinkage occurs during the elastic phase of initial deformation, with bending of the inclined and horizontal struts under load. Subsequently, the inclined struts produce plastic deformation, and the structure enters the stage of stress platform, where the layer-by-layer collapse phenomenon arises. With the further increase in loading displacement, the structure enters the yield stage, all the pillars bend and collapse, and the whole structure presents a densification state.

For the H-8 structure, when transverse shrinkage occurs, the vertical pillar of the middle two layers will tilt and the diagonal pillar will bend. The third and fourth layers will first collapse layer by layer, followed by the bottom two layers, and the top two layers will collapse finally, and the whole structure presents "wavy" densification. For the H-5.5 structure, plastic collapse and horizontal dislocation occur first at the top and bottom layers, and the overall structure gradually changes from "rectangle" to "diamond shape", followed by collapse of the middle two layers, and finally the second and fifth layers become dense. For the unidirectional gradient structure, the collapse occurs layer by layer from the direction of large gradient to the direction of small gradient, indicating that the small size structure has stronger stability and is more difficult to produce bending of the pillar. As for the bidirectional gradient structure, both structures also collapse layer by layer from the large-gradient direction to the small-gradient direction, which again verifies the stability and excellent deformation resistance of the small-size structure. The detailed deformation process is shown in Fig. 11.

4.2 Stress-Strain Behavior

Figure 12 shows the Stress-strain curves of all structures, from which it can be clearly observed that the compression process is mainly divided into elastic phase, stress plateau phase, and densification phase. In the elastic phase, the Stress-strain curves of all structures almost coincide, indicating that the gradient has little effect on the elastic phase of cellular structures.

When reaching the stress plateau phase, H-5.5 exhibited a high stress plateau phenomenon compared with other structures, indicating that the H-5.5 structure has the strongest load-bearing capacity. The H-8 structure has the lowest plateau stress, which indicates that the structure is more likely to bend and break the struts during the compression process and has the

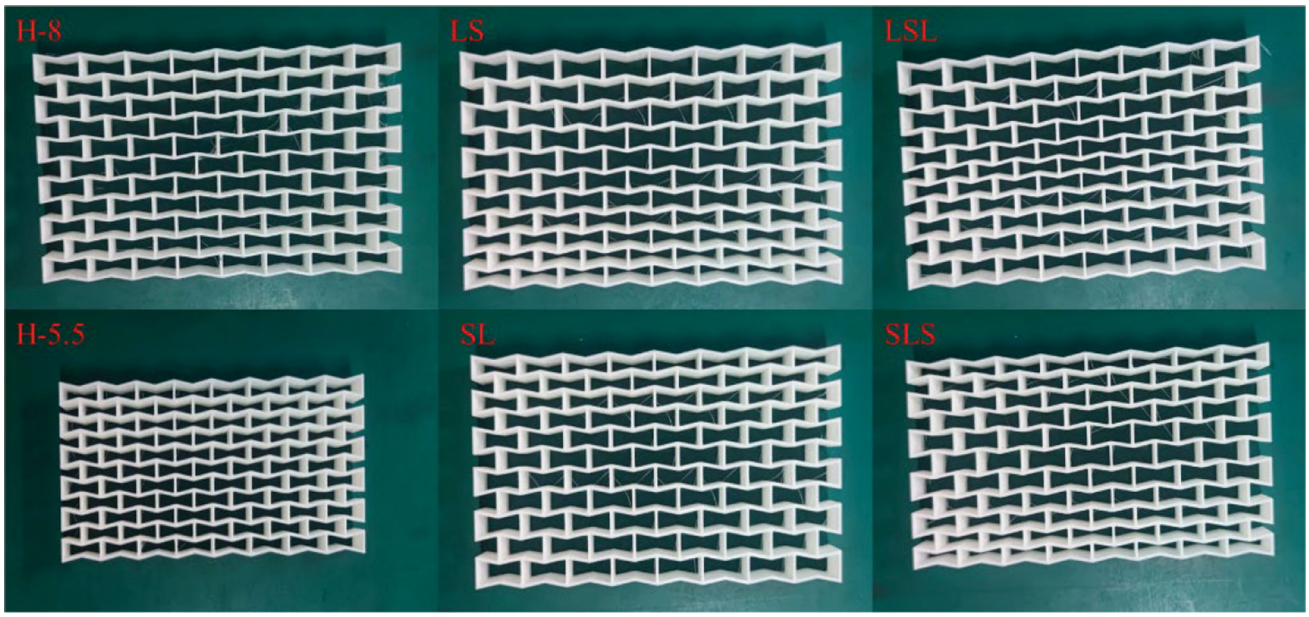

Fig. 9 The prepared specimens

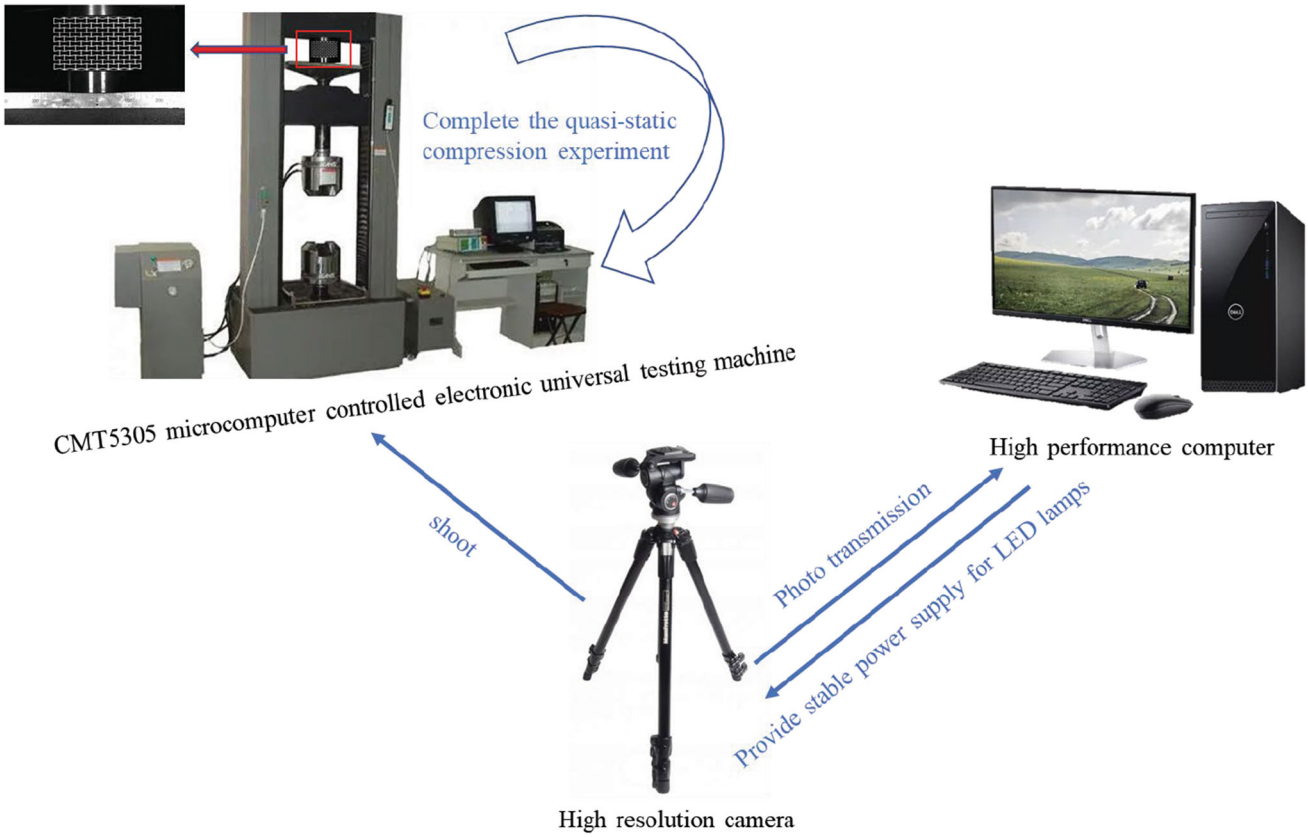

Fig. 10 Quasi-static compression test loading device

weakest resistance to deformation. For the gradient structure, the overall plateau stress of the bidirectional gradient structure is higher compared to the unidirectional gradient structure, indicating that the bidirectional gradient structure has a stronger ability to resist deformation during the stress plateau phase. Meanwhile, all structures have experienced a quasi-plateau phase in which the plateau stress increases gradually, among which the plateau stress phase is the longest for the H-8 structure and the shortest for the H-5.5 structure, while the gradient structure has little difference in the plateau stress phase. During the loading process of H-8, there are many sustained fractures of the struts in the plateau stress phase, corresponding to the continuous "wavy" curve in Fig. 12, which also confirms that the H-8 structure has the weakest ability to resist deformation.

The H-5.5 structure has the shortest plateau stress phase, so the structure enters the densification phase at the earliest, and the higher the corresponding stress value at the same strain value, which again indicates that the structure has the strongest load bearing capacity. The H-8 structure enters the densification phase the latest and enters the densification phase with low stress values due to the fracture of a large number of struts generated in the plateau stress phase, and thus the overall load bearing capacity is the lowest. After entering the densification phase, the overall load-bearing capacity of the gradient structure is SLS, SL, LSL, and LS in order from strong to weak. It shows that the closer the bearing end is to the small size structure, the stronger the overall load-bearing capacity will be after entering densification. For the same small size structure, the bidirectional gradient structure has stronger overall bearing performance compared to the unidirectional gradient structure.

4.3 Energy Absorption Performance

After the quasi-static compression experiments on the specimens, some theoretical indexes need to be selected to evaluate the energy absorption performance of the structure, and some common parameters such as specific energy absorption (SEA), dimensionless platform stress (DPS), mean crushing force (MCF) and crushing force efficiency (CFE) are selected to evaluate the energy absorption capacity of the structure.

As the variation in cell height causes the relative density of the structure to vary drastically in the gradient direction, to prevent the over influence of relative density over mechanical performances of various designs, the energy absorption performance of the structure should also be evaluated with the specific energy absorption to eliminate any discrepancies.

The SEA which eliminates the variation of mass in total energy absorption of various specimens, can be expressed through the total energy absorbed, which is the area under the load-displacement graph divided by the mass of the structure expressed as:

$$\mathrm{SEA}(L) = \frac{\mathrm{EA}(L)}{M} \qquad \text{(Eq 42)}$$

where M is the mass of the structure and L is the load displacement. $\mathrm{EA}(L)$ represents the total absorbed energy during quasi-static compression, which can be obtained from

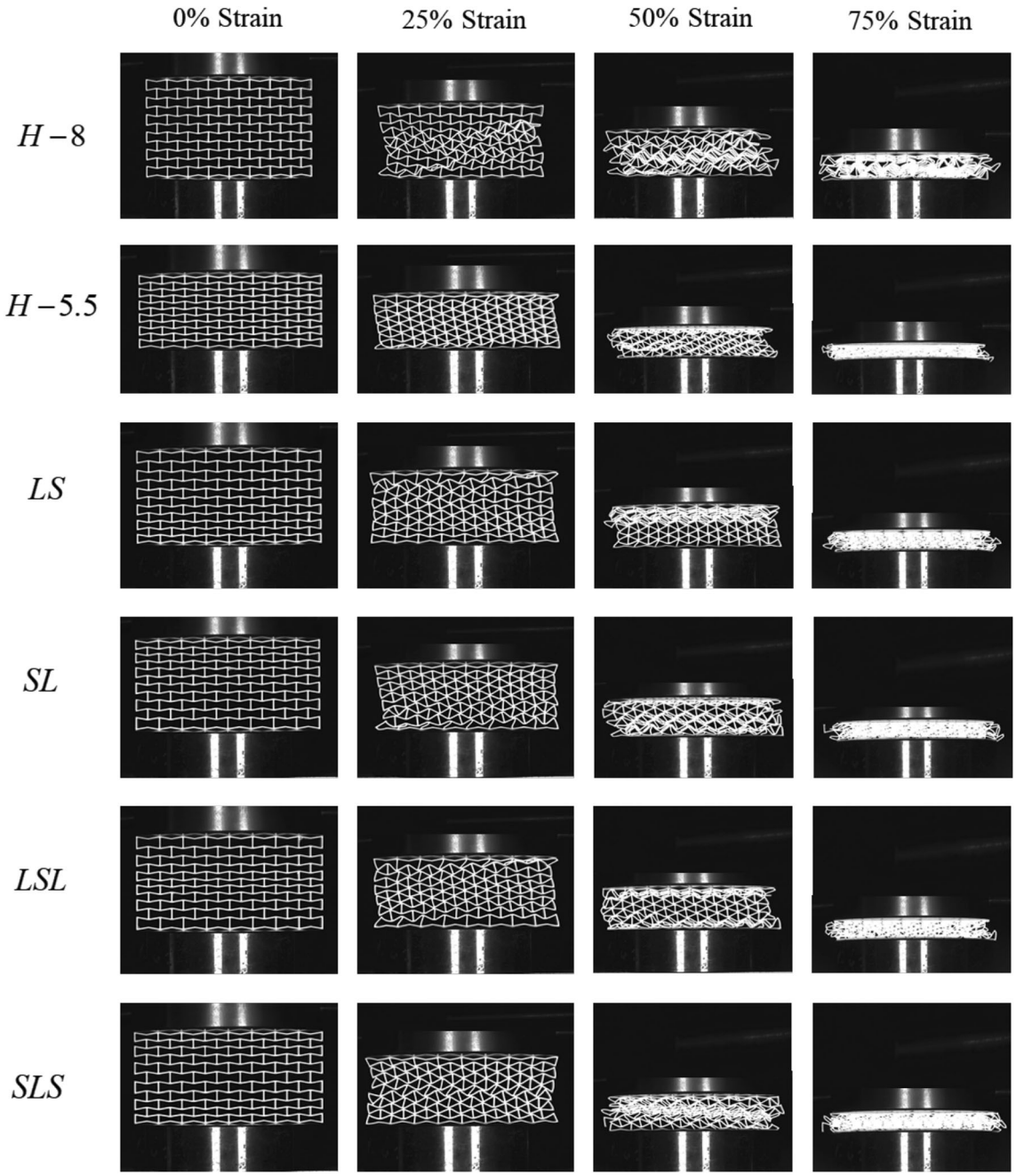

Fig. 11 Detailed deformation process of all structures

the integration of the loading load over the loading displacement.

$$\mathrm{EA}(L) = \int_0^L F(x)dx \qquad \text{(Eq 43)}$$

The MCF indicates the load carrying capacity of the structure during the quasi-static process, which can show the loading resistance of the structure to a certain extent, and its expression is as follows:

$$\mathrm{MCF} = \frac{\mathrm{EA}(L)}{L} \qquad \text{(Eq 44)}$$

The CFE, aimed to be closed 1, is defined as the MCF divided by the peak crushing force (PCF), and its expression is as follows:

$$\mathrm{CFE} = \frac{\mathrm{MCF}}{\mathrm{PCF}} \qquad \text{(Eq 45)}$$

The DPS σ_p reflects the impact strength of the structure, where A is the area of the top of the structure. To eliminate the effect of the material yield stress, the DPS σ_p can be obtained by dividing the material yield stress σ_s, and the expression is as follows:

$$\sigma_p = \frac{EA(L)}{L \times A \times \sigma_s} \qquad \text{(Eq 46)}$$

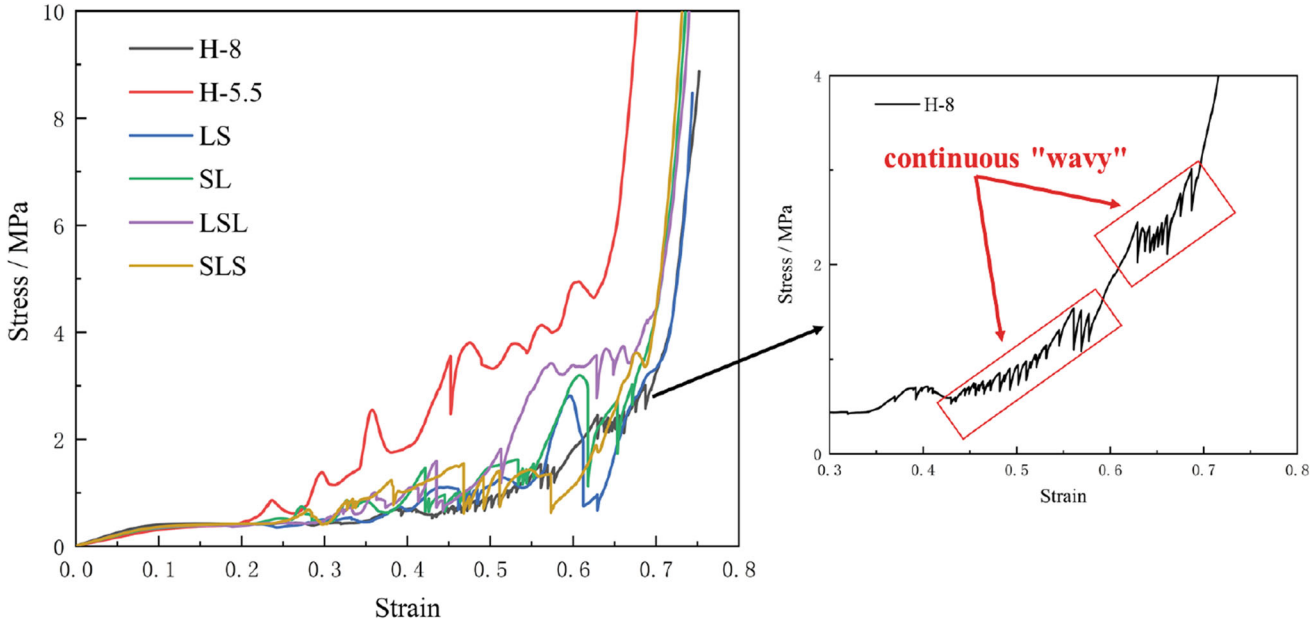

Fig. 12 The Stress-strain curves of all structures

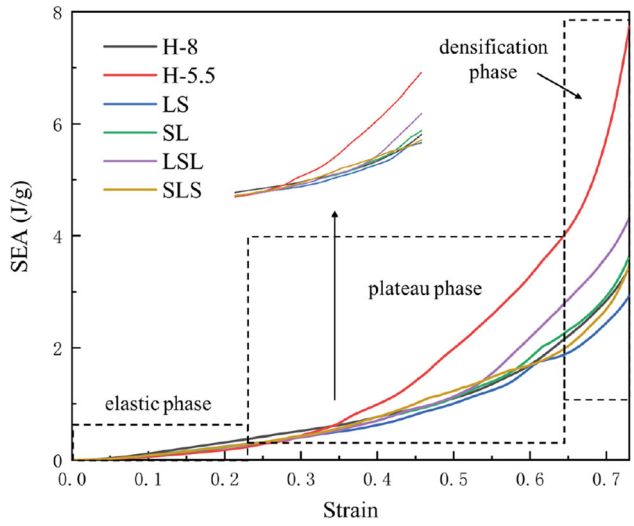

Fig. 13 The SEA curves of all structures

Figure 13 shows the SEA curves of the all structures, from which it can be observed that there is little difference at the elastic phase, which is consistent with the observation results in the load-displacement curve, indicating that the variation of unit height has no influence on the load carrying capacity and energy absorption performance of the structure in the elastic phase.

When reaching the plateau phase, the SEA of each structure starts to differ. H-5, due to the small cell size, will be more likely to deform and contact each other during the compression process, enhancing the overall pressure-bearing performance, thus always showing a higher SEA. H-8, due to the large cell space pores and thus a larger deformable range of the struts, shows relatively good SEA characteristics in the early stage of the plateau phase, while maintaining consistent SEA characteristics due to the uniformity of the structure. For the gradient structure, the SEA of the LSL and SL structures are comparable to the H-8, while the SEA of the SLS structure continues to increase, second only to the H-5.5, and the LS has the weakest SEA characteristics.

The H-5.5 structure still maintains its high SEA characteristics in the densification phase, while the LSL structure continues to increase its SEA characteristics during the densification phase since the upper and lower layers first collapse and thus squeeze each other, which is similar to adding horizontal surfaces at the top and bottom of the structure to resist deformation and is second only to the H-5.5 structure. The SEA of the SL, SLS, and H-8 structures are comparable, and the LS structure continues to be consistently stable, still the weakest among the six structures.

Figure 14 exhibits the MCF and DPS of all the structures, from which the H-5.5 structure has the strongest MCF and DPS, with an improvement of 147.80% in MCF and 147.93% in DPS compared to the weakest LS structure. Apart from this, the H-8 structure differs greatly from the H-5.5 structure, but higher than all gradient structures. This conclusion shows that the main reason for the discrepancy with the SEA conclusion is that the H-8 structure has 1.5 times more mass compared to the other structures, and therefore it shows larger MCF and DPS. For the gradient structure, the LSL structure has the highest MCF and DPS of 2.59 KN and 0.0216, respectively. SL structure and SLS structure have similar MCF and DPS, which are reduced by about 22%-25% compared with LSL structure. This trend is consistent with the above SEA conclusions, which mutually confirm the correctness of the conclusions obtained.

5. Conclusions

In this paper, analytical expressions of mechanical properties of auxetic cellular structures with spatial irregular configuration are obtained. The Euler-Bernoulli beam theory and multi-step bottom-up approach are considered for deriving the

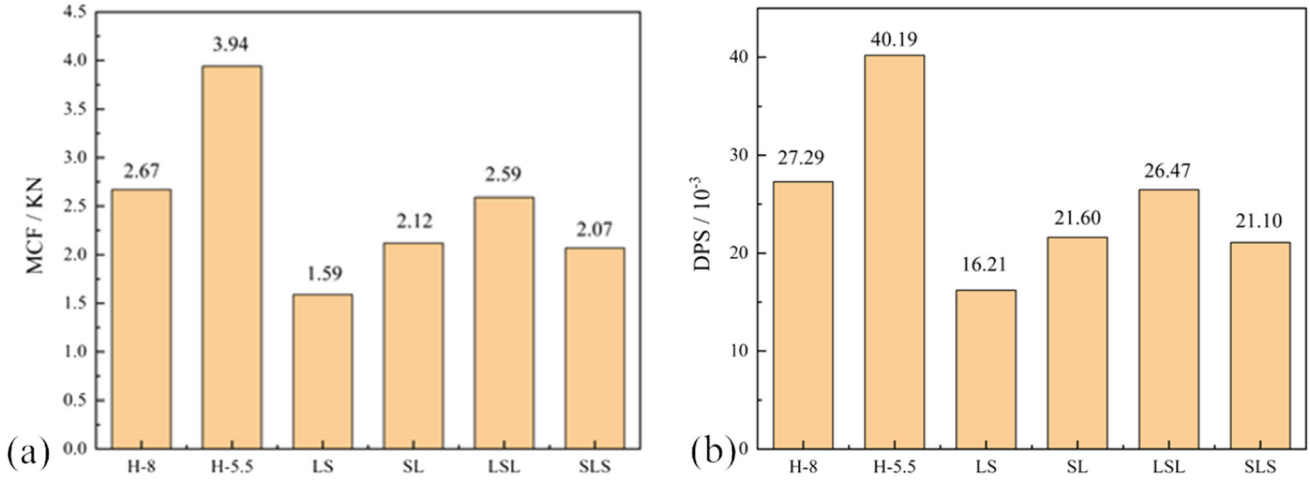

Fig. 14 The MCF and DPS of all structures

analytical relationships. In addition, the deformation pattern, stress-strain behavior, and energy absorption performance of the auxetic cellular structure with gradient cell height under quasi-static compressive loading are investigated.

The results suggested that:

(1) E_{1eq}/E_s decreases from 1.62942 to 1.16143 with the increase of h and increases from 39.28937 to 109.97178 with the increase θ, and the variation amplitude increases gradually. E_{2eq}/E_s increases from 0.0383 to 0.0632 with the increase of h and exhibits a continuous decrease with the increase of θ. υ_{12eq} increases from -8.68695 to -6.19194 with the increase of h and shows a trend of increasing and then decreasing with the increase of θ, while υ_{21eq} decreases from -0.115115 to -0.161500 with the increase of h and shows a trend of decreasing and then increasing with the increase of θ, and both obtain the maximum value at 19°.

(2) The failure of all structures is the layer-by-layer collapse of auxetic cellular structural cells, and the small-sized structures have stronger stability and are more difficult to produce strut bending.

(3) The gradient cell size has little effect on the elastic phase of stress-strain behavior and energy absorption performance.

(4) The bidirectional gradient structure has higher platform stress compared with the unidirectional gradient structure; the closer the bearing end is to the small size cell, the stronger the overall load-bearing capacity and the energy absorption performance of the structure becomes after densification.

(5) The H-5.5 structure has the strongest load-bearing capacity as well as energy-absorbing performance, and the LS structure has the weakest SEA, MCF and DPS. The H-8 structures exhibit different trends in MCF and DPS from SEA due to its larger mass.

(6) This paper only experimentally studied the failure mode, stress-strain behavior, and energy absorption performance of graded cellular structures under quasi-static loading and did not explore the mechanical properties of such structures under impact loading, so the research results have certain limitations. In the subsequent study, we can focus on the response of this type of structure under impact loading and analyze and discuss the results in comparison with those under quasi-static loading, to obtain the effect law of loading rate on the gradient cellular structure.

Acknowledgments

This research was supported by NSAF(U1930204).

Author Contributions

XZ: Conceptualization, Methodology, Writing-original draft, Writing-review&editing, Mechanical experiments, Data curation, Visualization. QD: Conceptualization, Formal analysis, Methodology, Resources, Funding acquisition, Supervision, Writing-original draft, Writing-review&editing. XS: Supervision. XL: Mechanical experiments, Supervision, Visualization.

Data Availability

Data will be made available on request.

Conflict of interest

The authors declare that they have no known competing financial interests or personal relationships that could have appeared to influence the work reported in this paper.

References

1. Q.T. Deng and Z.C. Yang, Effects of Poisson's Ratio on Functionally Graded Cellular Structures, *Mater. Express*, 2016, **6**(6), p 461–472
2. J.X. Qiao and C.Q. Chen, Impact Resistance of Uniform and Functionally Graded Auxetic Double Arrowhead Honeycomb, *Int. J. Impact Eng*, 2015, **83**, p 47–58
3. H. Mitschke, F. Schury, K. Mecke, F. Wein, M. Stingl, and G.E. Schroder-Turk, Geometry: The Leading Parameter for Poisson's Ratio of Bending-Dominated Cellular Solids, *Int. J. Solids Struct.*, 2016, **100–101**, p 1–10

4. N.S. Ha and G. Lu, A review of Recent Research on Bio-inspired Structures and Materials for Energy Absorption Applications, *Compos. Pt B-Eng.*, 2019, **181**, p 107496
5. D. Sharma and S.S. Hiremath, Bio-inspired Repeatable Lattice Structures for Energy Absorption: Experimental and Finite Element Study, *Compos. Struct.*, 2022, **283**, p 115102
6. Z. Liu, M.A. Meyers, Z. Zhang, and R.O. Ritchie, Functional Gradients and Heterogeneities in Biological Materials: Design Principles, Functions, and Bioinspired Applications, *Prog. Mater. Sci.*, 2017, **88**(1), p 467–498
7. A. Ingrole, T.G. Aguirre, L. Fuller, and S.W. Donahue, Bioinspired Energy Absorbing Material Designs Using Additive Manufacturing, *J. Mech. Behav. Biomed. Mater.*, 2021, **119**(5732), p 104518
8. S. Limmahakhun, A. Oloyede, K. Sitthiseripratip, Y. Xiao, and C. Yan, 3D-printed Cellular Structures for Bone Biomimetic Implants, *Addit. Manuf.*, 2017, **15**, p 93–101
9. Y. Kun, T. Fei, W.Y. Bo, and H. YH. Study on Impact Energy Absorption Performance and Optimization of Negative Poisson's Ratio Structure. J. Mech. Behav. Biomed. Mater. 2023, **45**(6), p 328
10. N.F. Ma, Q. Han, S.H. Han, and C.L. Li, Hierarchical Re-entrant Honeycomb Metamaterial for Energy Absorption and Vibration Insulation, *Int. J. Mech. Sci.*, 2023, **250**, p 108307
11. X. Ren, R. Das, P. Tran, T.D. Ngo, and Y.M. Xie, Auxetic Metamaterials and Structures: A Review, *Smart Mater. Struct.*, 2018, **27**(2), p 023001
12. R. Hedayati, M. Sadighi, M. Mohammadi-Aghdam, and A.A. Zadpoor, Mechanical Properties of Additively Manufactured Octagonal Honeycomb, *Mater. Sci. Eng. C-Mater Biol. Appl.*, 2016, **69**, p 1307–1317
13. P. Zhang, J. Toman, Y.Q. Yu, E. Biyikli, M. Kirca, and M. Chmielus, Efficient Design-optimization of Variable-density Hexagonal Cellular Structure by Additive Manufacturing: Theory and Validation, *J. Manuf. Sci. Eng-Trans. ASME*, 2015, **37**, p 021004
14. L. Yang, C.Z. Yan, C.J. Han, P. Chen, S.F. Yang, and Y.S. Shi, Mechanical Response of a Triply Periodic Minimal Surface Cellular Structures Manufactured by Selective Laser Melting, *Int. J. Mech. Sci.*, 2018, **148**, p 149–157
15. X.R. Zhang, Q.T. Deng, X.B. Li, and X.L. Song, Study on Crack Propagation of Plane Cellular Structure, *J. Plast. Eng.*, 2022, **29**, p 158–167
16. X.R. Zhang, Q.T. Deng, X.B. Li, J.P. Wen, and X.L. Song, Influence of Prefabricated Crack Parameters and Relative Density on Crack Propagation in Planar Cellular Structures, *J. Exp. Mech.*, 2023, **38**, p 68–80
17. M.S. Tatl, A Comparative Analysis of the In-plane Energy Absorption Capacities of Auxetic Structures, *Trans. Can. Soc. Mech. Eng.*, 2022, **46**(2), p 216–224
18. N. Novak, M. Vesenjak, S. Tanaka, K. Hokamoto, and Z. Ren, Compressive Behaviour of Chiral Auxetic Cellular Structures at Different Strain Rates, *Int. J. Impact Eng*, 2020, **141**, p 103566
19. Z. Lu, Q. Wang, X. Li, and Z.Y. Yang, Elastic Properties of Two Novel Auxetic 3D Cellular Structures, *Int. J. Solids Struct.*, 2017, **124**, p 46–56
20. R. Valle, G. Pincheira, and V. Tuninetti, Design of an Auxetic Cellular Structure with Different Elastic Properties in its Three Orthogonal Directions, *Proc. Inst. Mech. Eng. Pt L-J Mater-Design Appl.*, 2021, **235**(6), p 1341–1350
21. Y. Bai, T. Zhao, C. Yuan, W.D. Liu, H.C. Zhang, L. Yang, and C.M. She, Mechanical Properties of a Chiral Cellular Structure with Semicircular Beams, *Materials*, 2021, **14**(11), p 2887
22. W. Liu, H. Li, J. Zhang, and H.D. Li, Elastic Properties of a Novel Cellular Structure with Trapezoidal Beams, *Aerosp. Sci. Technol.*, 2018, **75**, p 315–328
23. Q. Gao, Z. Ding, and W.H. Liao, Effective Elastic Properties of Irregular Auxetic Structures, *Compos. Struct.*, 2022, **287**, p 115269
24. W. Hou, X. Yang, W. Zhang, and X. Yang, Design of Energy-dissipating Structure with Functionally Graded Auxetic Cellular Material. Int. J. Crashworthiness 2017, 1–11
25. D.W. Li, W.H. Liao, N. Dai, G.Y. Dong, Y.L. Tang, and Y.M. Xie, Optimal Design and Modeling of Gyroid-based Functionally Graded Cellular Structures for Additive Manufacturing, *Comput-Aided Des.*, 2018, **104**, p 87–99
26. N. Novak, M. Vesenjak, and Z.R. Ren, Computational Simulation and Optimization of Functionally Graded Auxetic Structures Made from Inverted Tetrapods, *Phys. Status Solidi B-Basic Solid State Phys.*, 2017, **254**(12), p 1600753
27. H. Niknam, A.H. Akbarzadeh, D. Rodrigue, and D. Therriault, Architected Multi-directional Functionally Graded Cellular Plates, *Mater. Des.*, 2018, **148**, p 188–202
28. A. Ajdari, H. Nayeb-Hashemi, and A. Vaziri, Dynamic Crushing and Energy Absorption of Regular, Irregular and Functionally Graded Cellular Structures, *Int. J. Solids Struct.*, 2011, **48**, p 506–516
29. D. Li, W. Liao, N. Dai, and Y.M. Xie, Comparison of Mechanical Properties and Energy Absorption of Sheet-Based and Strut-Based Gyroid Cellular Structures with Graded Densities, *Materials*, 2019, **12**(13), p 2183
30. T. Mukhopadhyay and S. Adhikari, Effective In-plane Elastic Properties of Auxetic Honeycombs with Spatial Irregularity, *Mech. Mater.*, 2016, **95**, p 204–222
31. T. Mukhopadhyay and S. Adhikari, Effective In-plane Elastic Moduli of Quasi-random Spatially Irregular Hexagonal Lattices, *Int. J. Eng. Sci.*, 2017, **119**, p 142–179
32. F. Zhu, H.B. Xiao, Y.G. Xue, X. Feng, Y.G. Huang, and Y.J. Ma, Anisotropic Mechanics of Cellular Substrate Under Finite Deformation, *J. Appl. Mech.*, 2018, **85**, p 071007
33. L.J. Gibson and M.F. Ashby, *Cellular Solids: Structure and Properties*, Cambridge University Press, Cambridge, 1997